

A. T. Motta,¹ M. J. Gomes da Silva,¹ A. Yilmazbayhan,¹ R. J. Comstock,² Z. Cai,³ and B. Lai³

Microstructural Characterization of Oxides Formed on Model Zr Alloys Using Synchrotron Radiation

ABSTRACT: To understand how alloy chemistry and microstructure impact corrosion performance, oxide layers formed at different stages of corrosion on various model zirconium alloys (Zr-xFe-yCr, Zr-xCu-yMo, for various x, y) and control materials (pure Zr, Zircaloy-4) were examined to determine their structure and the connection of such structure to corrosion kinetics and oxide stability. Microbeam synchrotron radiation diffraction and fluorescence of oxide cross sections were used to determine the oxide phases present, grain size, and orientation relationships as a function of distance from the oxide-metal interface. The results show a wide variation of corrosion behavior among the alloys, in terms of the pretransition corrosion kinetics and in terms of the oxide susceptibility to breakaway corrosion. The alloys that exhibited protective behavior at 500°C also were protective during 360°C corrosion testing. The Zr-0.4Fe-0.2Cr model ternary alloy showed protective behavior and stable oxide growth throughout the test. The results of the examination of the oxide layers with microbeam X-ray diffraction show clear differences in the structure of protective and nonprotective oxides both at the oxide-metal interface and in the bulk of the oxide layer. The nonprotective oxide interfaces show a smooth transition from metal to oxide with metal diffraction peaks disappearing as the monoclinic oxide peaks appear. In contrast, the protective oxides showed a complex structure near the oxide-metal interface, showing peaks from Zr₃O suboxide and a highly oriented tetragonal oxide phase with specific orientation relationships with the monoclinic oxide and the base metal. The same interfacial structures are observed through their diffraction signals in protective oxide layers formed during both 360°C and 500°C corrosion testing. These diffraction peaks showed much higher intensities in the samples from 500°C testing. The results for the various model alloys are discussed to help elucidate the role of individual alloying elements in oxide formation and the influence of oxide microstructure on the corrosion mechanism.

KEYWORDS: zirconium alloys, corrosion, x-ray diffraction, oxide phases

Introduction

Minimizing waterside corrosion of Zr-based alloys remains an important issue for the utilization of these alloys as fuel cladding and structural components in light water reactors [1]. Increases in coolant temperature, power uprates, extended burnups, and longer residence times have resulted in the development of advanced Zr alloys to meet the needs of nuclear power plant operators [2,3]. Despite the successful application of advanced Zr alloys with improved corrosion behavior, full understanding of the corrosion mechanism and of the role of alloy additions on corrosion remains elusive.

Prior work revealed the periodic nature of zirconium alloy corrosion in which oxide layers of a constant thickness were observed across the entire oxide thickness [4]. The presence of a layered oxide structure suggested that corrosion proceeded by a repetitive process of oxide growth to a critical thickness followed by a transition to the growth of the next oxide layer. This repetitive growth of oxide layers can be characterized as stable growth with each layer growing as a protective oxide with a decrease in growth rate with increased thickness.

Layered oxide structures were observed in Zircaloy-4, ZIRLO™, and Zr-2.5Nb alloys following autoclave exposures in 633 K water [4–6]. In addition, the oxide layers were characterized by columnar grains that were oriented along the growth direction with a preferred crystallographic texture. While the oxides exhibited several common features (layers, columnar grains, texture), small differences in the

Manuscript received May 30, 2005; accepted for publication January 9, 2008; published online March 2008. Presented at ASTM Symposium on Zirconium in the Nuclear Industry: 15th International Symposium on 24–28 June 2007 in Sunriver, OR; Magnus Limback and Bruce Kammenzind, Guest Editors.

¹ Department of Mechanical and Nuclear Engineering, The Pennsylvania State University, University Park, PA 16802.

² Science and Technology Department, Westinghouse Electric Co., Pittsburgh, PA 15235.

³ Advanced Photon Source, Argonne National Laboratory, Argonne, IL 60439.

magnitude of these features were observed in the more corrosion-resistant alloys (lower post-transition corrosion rates) exhibiting thicker oxide layers with larger columnar grains [7]. In contrast to the above stable growth, breakaway oxide growth occurred in Zircaloy-4 and Zr-2.5Nb when tested in 633 K water containing 70 ppm Li. Breakaway growth was characterized by a rapid increase in corrosion rate and no discernible oxide layers. Additional oxide characteristics included equiaxed grains and porosity extending to the oxide-metal interface. Breakaway oxide growth began immediately in Zr-2.5Nb while breakaway growth occurred in Zircaloy-4 following a period of stable growth. It is noteworthy that ZIRLO exhibited stable growth in lithiated water and unlike the oxides formed on Zircaloy-4 and Zr-2.5Nb, the oxide was layered with reduced porosity at the oxide-metal interface [7].

The above approach to understanding the differences in corrosion behavior of zirconium-based alloys focused on characterization of the oxide microstructure. However, in commercial alloys it is difficult to separate the roles of individual alloying elements on corrosion. In the present study, a series of various model zirconium alloys were prepared and corrosion tested in 360°C pure water, 500°C steam, and 500°C supercritical water. The model alloys were chosen to highlight the role of alloy additions on the corrosion process. Oxides formed on the model alloys were examined to identify oxide features that were characteristic of stable oxide growth (formation of repetitive protective layers) or breakaway growth (formation of nonprotective oxide). Previous studies have also focused on the behavior of model alloys [8], but here these studies are expanded on by (a) generating a more detailed study of corrosion kinetics (with more data points), and (b) characterizing the structure of the oxide layers using advanced techniques to relate oxide structure to corrosion kinetics and oxide stability.

Experimental Methods

Model Alloys

A series of binary and ternary model alloys was prepared in the context of a broader study of the effect of alloying elements on the formation of a protective oxide layer on Zr alloys during waterside corrosion [9]. The alloying elements were precipitate-forming elements such as Fe, Cr, Cu, and Mo, and two elements that form extensive solid solutions with Zr: Sn and Nb (it is recognized that Nb also forms precipitates at concentrations above the solubility limit of about 0.4–0.5 %). This study focuses primarily on the characterization and study of the oxide layers formed on the samples of the precipitate-forming alloys during corrosion testing in 360°C water, 500°C steam, and 500°C supercritical water. The alloys were selected to highlight the individual role of alloying elements in the formation of a stable protective oxide during waterside corrosion. For example, the specific Zr-Fe-Cr alloys chosen highlight separately the roles of precipitate volume fraction and of precipitate size. Thus a set of four model alloys were prepared in which the volume fraction was increased by increased alloy content and the precipitate size by longer and higher temperature anneals [10]. The comparison of the corrosion results in these alloys with those in standards and in pure Zr should give insight into the mechanisms of alloying protection.

Table 1 lists the target and measured compositions of the alloys used in this study. These alloys were prepared by arc melting 350-g button ingots multiple times to ensure chemical homogeneity. The arc-melted ingots were beta-solution treated at 1050°C, water quenched, hot-rolled, given two iterations of intermediate annealing and cold-rolling to reach final size (0.8 mm), and then final annealed. The thermal processing following the water quench was performed at a single temperature (580°C, 650°C, or 720°C) for each button ingot.

The main groups contained alloys that form second phase particles (Zr-Fe-Cr alloys, Zr-Cr-Fe alloys, Zr-Cu-Mo), in addition to pure Zr (sponge and crystal bar) and Zircaloy-4 (a Zircaloy-4 sample was melted and processed in the same way as the model alloys). The second phase particles found in each alloy, were identified using synchrotron radiation X-ray diffraction as done previously for Zircaloy [10,11].

Corrosion Testing

Specimens for corrosion testing, measuring 25 mm by 20 mm by 0.8 mm, were cut from the manufactured strip, mechanically ground using 1200 grit SiC paper, and then pickled in a solution of 5 vol. % HF, 45 vol. % HNO₃, and 50 vol. % H₂O. The corrosion tests were conducted in 360°C water,

TABLE 1—Chemical composition of alloys studied.

Alloy System	Target Alloy Additions (wt %)	Measured Chemistry (wt ppm)						Process Temperature (C)
		Nb	Sn	Fe	Cr	Cu	Mo	
Zr-Fe-Cr	0.2Fe-0.1Cr	<20	<80	1843	913	19	<10	580 (L) and 720 (H)
	0.4Fe-0.2Cr	<20	<80	4013	1971	<10	<10	580 (L) and 720 (H)
Zr-Cr-Fe	0.5Cr	<20	<80	179	4808	<10	<10	650
	0.5Cr-0.2Fe	<20	<80	1958	4907	<10	<10	650
	1.0Cr	<20	<80	189	9265	<10	<10	650
	1.0Cr-0.2Fe	<20	<80	1862	9292	115	11	650
Zr-Cu-Mo	0.5Cu	0	<80	195	21	4538	<10	580
	0.5Cu-0.5Mo	0	<80	192	20	4774	4699	580
	1.0Cu	0	<80	194	22	10634	<10	580
	1.0Cu-0.5Mo	0	<80	183	20	9954	4629	580
Reference	Sponge Zr	<20	<80	184	23	<10	<10	580
	Crystal bar Zr	<20	<80	116	20	<10	<10	580
	Zircaloy-4	<20	13060	1981	1085	26	<10	580

500°C/10.3 MPa steam, and 500°C/24.1 MPa supercritical water (SCW) in a manner consistent with the ASTM Practice G2/G2M-06 “Standard Test Method for Corrosion Testing of Products of Zirconium, Hafnium, and Their Alloys in Water at 680°F [360°C] or in Steam at 750°F [400°C]. The corrosion behavior of the specimens was evaluated by measuring the weight gain as a function of the exposure time. The corrosion test in supercritical water was performed in a dynamic loop system (water is constantly refreshed, and chemistry is controlled) at the University of Michigan. The 360°C water and 500°C steam corrosion tests were performed at Westinghouse in static autoclaves. The details of the testing were previously given in Ref. [10]. At least 16 samples from each model alloy were prepared, to allow careful measurement of pretransition kinetics and to provide good statistics. Samples were systematically removed from the autoclave for weight gain measurements and occasionally archived for microstructure examination. Frequent weight gain measurements were performed in the early part of the corrosion test to determine the corrosion kinetics in the pretransition regime.

Microbeam Synchrotron Radiation X-ray Diffraction and Fluorescence

The corrosion coupons removed from the autoclave were cut into thin (1 mm) strips which were then inserted into thin-wall 3-mm diameter brass tubes [4]. Cross section slices cut from these tubes were mechanically ground and polished using successively finer abrasive media to 0.1 μm diamond. The oxide cross section samples were examined by micro-beam synchrotron radiation at the 2-ID-D beam line of the Advanced Photon Source at Argonne National Laboratory.

The microbeam was focused to a size of 0.25 μm in the vertical direction (normal to the oxide-metal interface) and had a 2- μm footprint in the horizontal direction (parallel to the oxide-metal interface). The beam energy was 9.5 keV, corresponding to a wavelength of 0.1305 nm. Diffraction and fluorescence data were simultaneously collected from the sample as it was translated across the beam in step sizes ranging from 0.15 to 0.50 μm . The diffraction data were collected by a flat two-dimensional detector (CCD camera), while the fluorescence data were collected by an energy dispersive detector.

The position of the microbeam within the oxide layers was determined by monitoring Zr L line fluorescence counts as the sample was translated across the beam [5]. The distance between the oxide-metal interface and the oxide-water interface measured by this method was in good agreement, most often to within 0.5 μm , with the optical determination of the oxide thickness. To obtain quantitative diffraction data, the digital data obtained from the two-dimensional detector were integrated over the elliptical sections for a fixed azimuthal angle, and the appropriate Lorentz and polarization correction factors were applied [4] to obtain a plot of diffracted intensity versus two-theta angle at each location analyzed. The peak positions of the phases identified corresponded with the peak positions in the respective powder diffraction files with a precision of a few hundredths of a degree in two-theta [12].

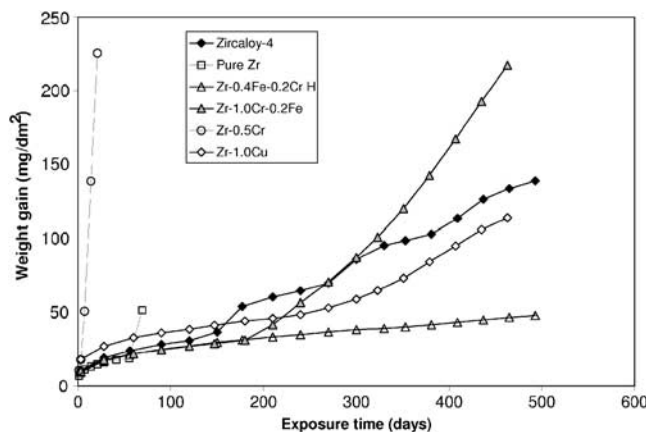


FIG. 1—Corrosion weight gain versus exposure time for model and reference alloys autoclaved in 360°C pure water.

Results

This section describes both the corrosion results and the results of microbeam diffraction oxide characterization of the oxide layers.

Corrosion in 360°C Water

The testing in 360°C water showed wide differences in behavior among the alloys, some showing protective behavior throughout the test, some showing immediate breakaway and some showing breakaway and loss of protectiveness after an initial period of protective behavior.

Figure 1 shows the corrosion weight gains of individual corrosion coupons of representative alloys (14.7 mg/dm² corresponds to one micron of oxide thickness). Focusing first on Zircaloy-4, it is possible to see that the corrosion weight gain exhibits the periodic behavior previously seen in this alloy. Three transitions are seen, with subsequent recovery of protective behavior. The oxide thickness at transition was about two microns, which corresponds well with previous oxide transition thickness measurements [5]. Zr-0.4Fe-0.2Cr (H) exhibited the best behavior of all of the alloys, showing a weight gain of about 48 mg/dm² after testing for 493 days. A similar alloy, but with lower alloying element content, and annealed at a lower temperature, (Zr-0.2Fe-0.1Cr (L)) showed identical behavior up to about 200 days then showed an increased rate of corrosion, without recovering protective behavior. This was also the behavior of the alloys Zr-1.0Cr-0.2Fe and Zr-1.0Cu shown in Fig. 1. The corrosion weight gains for sponge and crystal bar Zr showed large variability. Some coupons exhibited immediate breakaway behavior, while others showed protective behavior for up to 40 days and then showed breakaway behavior. The weight gain for one of these initially protective coupons is shown in Fig. 1. Finally, in some cases, such as occurred in some of the coupons of alloy Zr-0.5Cr, immediate breakaway behavior was seen: the weight gain for the coupon shown in Fig. 1 was 225 mg/dm² after 21 days.

When examined in the scanning electron microscope (SEM), these oxide layers showed wide variations of morphology, as shown in Fig. 2. Zircaloy-4 (Fig. 2(a)) shows periodic layers consistent with the transition thickness estimated from the weight gain curves, while the oxide layer for Zr-0.4Fe-0.2Cr (H) (Fig. 2(b)) showed a homogeneous oxide layer with little thickness variation. The nonprotective oxide layer formed on Zr-0.5Cr (Fig. 2(c)) showed extensive lateral cracking and a scalloped interface. This oxide layer exhibited “veins” (see figure) as previously reported in oxides formed at high burnup [13,14], showing the same association of veins with regions of lesser advance of the oxide. It has been conjectured previously that such veins result from the growth process of the oxide, and minimization of stress [13], but no systematic observations were made in this study to shed further light on this matter. In contrast, the oxide layers formed on pure Zr after breakaway showed a very uneven interface with dendrites of oxide advancing into the metal and very extensive cracking, as shown in Fig. 2(d). As discussed below, this interface instability for pure Zr is attributed to lateral variations in oxide characteristics due the absence of the homogenizing effect of alloying elements.

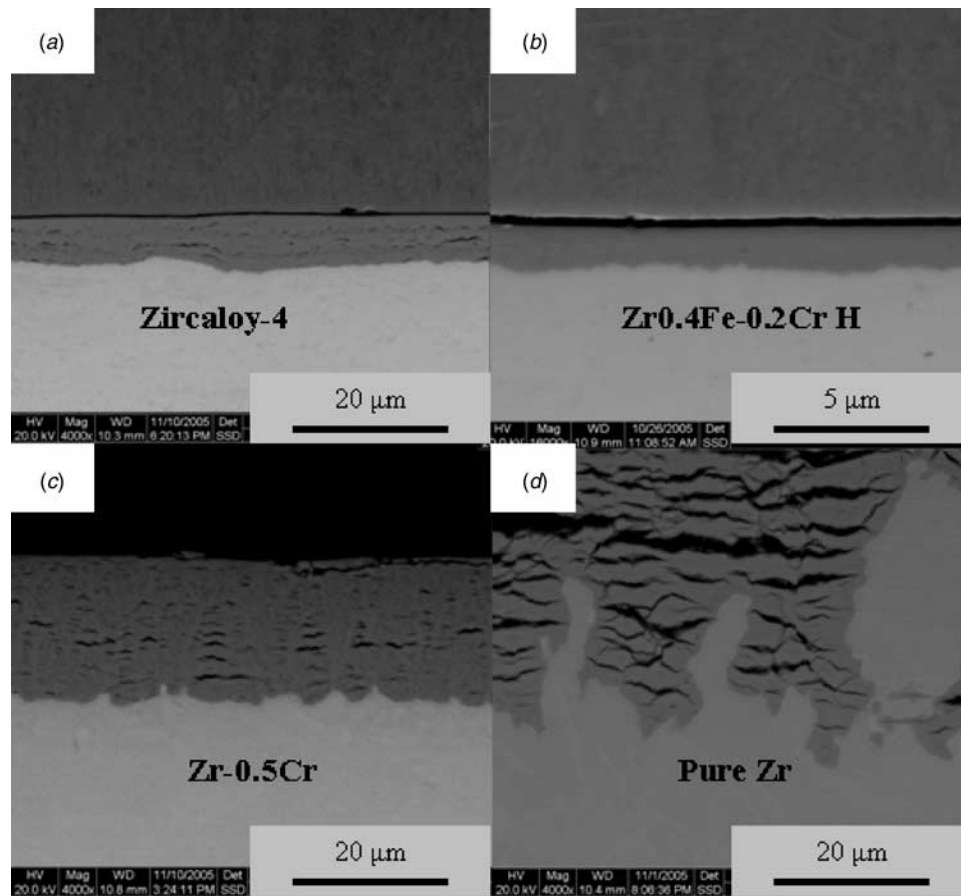


FIG. 2—SEM micrographs of oxide layers formed 360°C pure water. (a) Stable oxide layers on Zircaloy-4 (353 days, 104 mg/dm²), (b) stable oxide layer on Zr-0.4Fe-0.2Cr (H) (55.3 days, 24 mg/dm²), (c) breakaway oxide Zr-0.5Cr (14 days, 155 mg/dm²), and (d) breakaway oxide on crystal bar Zr (3 days, 6.2 mg/dm² with oxide spallation).

Corrosion in 500°C Steam and SCW

The corrosion results at 500°C also showed a wide spread in corrosion rate between the alloys [10]. Compared to the samples corroded during 360°C water testing, the samples corroded in 500°C supercritical water and 500°C steam showed much higher corrosion rates with a higher percentage of alloys exhibiting unstable oxide growth and breakaway. Although the corrosion rates were higher, surprisingly some of the alloys did exhibit protective oxide growth in both supercritical water and in steam throughout the duration of the tests. The corrosion weight gain at 500°C for some of the best performing alloys is shown in Fig. 3. The set of alloys that exhibited the best behavior during testing at 500°C was similar to that which exhibited good behavior during 360°C corrosion testing, the best alloys being in the Zr-Fe-Cr alloy group. Zircaloy-4 showed nonprotective behavior from the start of the 500°C test, as previously reported. Only small differences were seen between the steam and supercritical water results.

Corrosion Kinetics in the Pretransition (Protective) Regime

The corrosion weight gain can be characterized by two main factors: (a) the corrosion rate in the protective (pretransition) regime, and (b) the tendency to undergo transition or breakaway corrosion, or both. To characterize the corrosion in the protective regime, the weight gain curves in the protective regime were fit according to the following equation:

$$w = At^n \quad (1)$$

where w is the weight gain in mg/dm², t is the exposure time in days, and A and n are constants which are alloy dependent. Frequent weight gain measurements were taken at the beginning of the corrosion test and the fits obtained from the alloys exhibiting protective behavior were quite consistent from different cou-

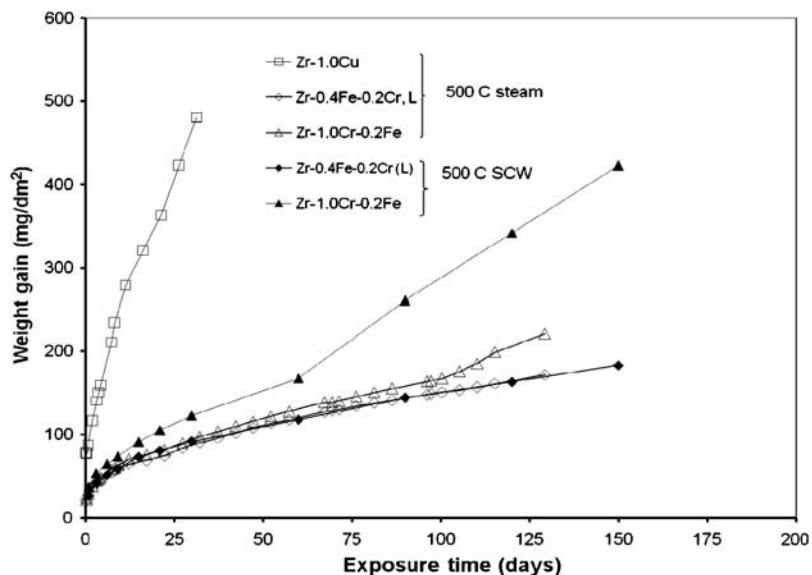


FIG. 3—Corrosion weight gain versus exposure time for model alloys autoclaved in supercritical water or steam at 500°C.

pons of a same alloy. The power law equation consistently fits the weight gain curves with confidence factors above 0.99. One example is shown in Fig. 4. Similar fits were obtained for all of the alloys and coupons that exhibited protective behavior.

The results of this fitting process are shown in the bar charts in Fig. 5 which plots the values of the exponent n (for corrosion at 360 and 500°C, in Figs. 5(a) and 5(b)) and the preexponential term A (Figs. 5(c) and 5(d) for 360 and 500°C) for the various alloys studied. Data generated on Zr-Nb and Zr-Nb-Sn systems by Jeong and co-workers are included for comparison [10,12]. The values of n come from the fitting of the weight gains of various individual coupons for a given alloy. The solid bars show the average value while the lines show the spread. This allows an evaluation of the spread of the values, which, as mentioned above, is small. The values of both A and n were higher at 500°C than at 360°C reflecting the faster corrosion kinetics at that temperature.

It is noteworthy also that the values of n appear to be dependent on the alloy. For testing at 360°C, the Zr-Nb samples show near parabolic behavior, with $n \cong 0.45$. The Zr-Nb-Sn samples show a slightly lower value of n and Zr-Sn lower still. The Zr alloys containing transition metal, (ZrFeCr, ZrCrFe, ZrCuMo, Zircaloy-4), in addition to pure Zr, showed values of n in the range of 0.20–0.25. At higher temperature, the ZrNb samples show supra-parabolic behavior while the ZrFeCr samples that behave in a protective manner show near-cubic behavior ($n=0.33$). It is interesting to note that ZrNb alloys (which form an

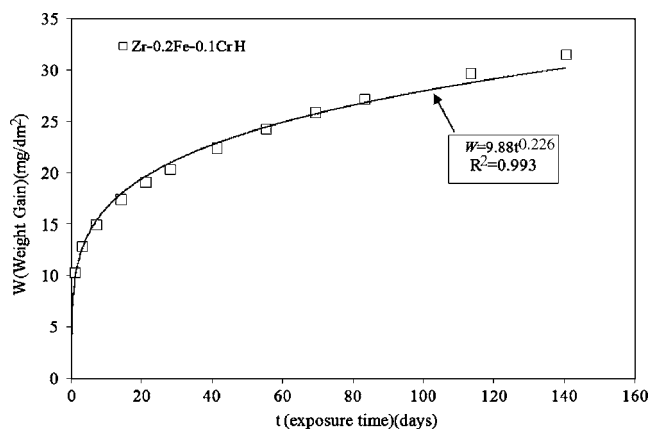


FIG. 4—Fit of pretransition weight gain versus exposure time data to a power law equation for Zr-0.2Fe-0.1Cr (H). The best fit and fitting parameter are indicated.

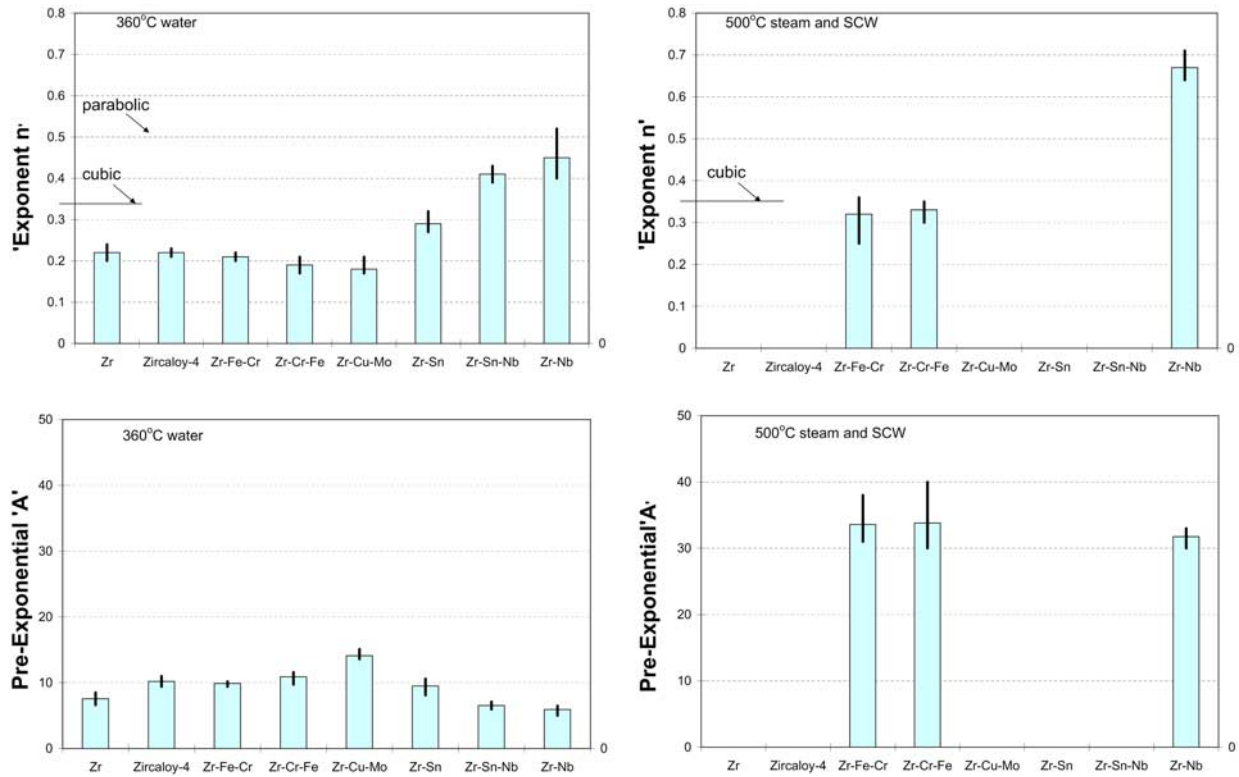


FIG. 5—Values obtained for the fitting parameters of the weight gain curves in the pretransition regime for the alloys examined in this study. (a) Exponent n at 360°C; (b) exponent n at 500°C; (c) pre-exponential A at 360°C and (d) pre-exponential A at 500°C.

extensive solid solution, since up to 0.4 Nb can dissolve in the matrix) show more nearly parabolic behavior than alloys that form little solid solution (the solubility of Fe, Cr, Cu, Mo in Zr is very low).

In addition to these differences in the pretransition corrosion kinetics, the alloy oxides also showed differences in their tendency to undergo either transition or breakaway corrosion. These are summarized in Table 2. The characterization efforts to rationalize these corrosion differences in terms of differences in the structure of the oxides are described in the next section.

Microbeam Diffraction Results

The corrosion samples of the model alloys archived at various stages of the corrosion process (and thus with oxide layers formed during protective and nonprotective regimes), were examined using microbeam synchrotron radiation diffraction, as was previously done for commercial alloys [4].

The diffraction patterns obtained from the oxide layers and their variation with oxide layer thickness were similar to those obtained in commercial alloys and showed many similarities between the protective and nonprotective oxide layers. However, they also showed significant and systematic differences.

The features that were common to all alloy oxides at both corrosion temperatures were the following:

1. The oxide layers consisted mostly of monoclinic ZrO_2 , with a small percentage of bulk tetragonal ZrO_2 . The tetragonal phase was seen throughout the oxide but with a higher percentage near the oxide-metal interface. The overall tetragonal phase content varied between the alloys.
2. The oxides were heavily textured, with the monoclinic oxide showing a growth direction close to the normal of the $(-301)_m$ plane. (In this paper, oxide peaks are written with a subscript m for monoclinic oxide and a subscript t for tetragonal oxide.) This is close to the growth direction (normal to the $(-601)_m$ plane) calculated by Li and co-workers [15] that minimizes stress accumulation. Other researchers have seen growth directions close to $(-401)_m$ [16,17].
3. Grain size did not vary significantly between alloys (although the grains were larger in oxide layers formed in 500°C testing). The grain sizes calculated from the full width half maximum of

TABLE 2—Summary corrosion results in 360°C water and in 500°C supercritical water and steam.

Alloy System	Chemistry	Corrosion Behavior in 360°C Water	Corrosion Behavior in 500°C SCW and Steam
Zr-Fe-Cr	0.2Fe-0.1Cr 0.4Fe-0.2Cr	<ul style="list-style-type: none"> • Protective, stable oxide growth for 0.2Fe-0.1Cr (580°C) through ~200 days followed by onset of nonprotective behavior • Protective, stable growth for remaining alloys through ~500 days (max. test duration). 	<ul style="list-style-type: none"> • Nonprotective, breakaway for 0.2Fe-Cr0.1Cr • Protective, stable oxide growth for higher alloying content (0.4Fe-0.2Cr)
Zr-Cr-Fe	0.5Cr 0.5Cr-0.2Fe 1.0Cr 1.0Cr-0.2Fe	<ul style="list-style-type: none"> • Initial stable oxide growth followed by breakaway growth • Fe addition was beneficial • 1.0Cr-0.2Fe showed longest time of stable growth before onset of breakaway 	<ul style="list-style-type: none"> • Protective behavior for 1.0Cr-0.2Fe suggesting benefit of Fe addition and high alloying content • Nonprotective behavior for remaining alloys
Zr-Cu-Mo	0.5Cu 0.5Cu-0.5Mo 1.0Cu 1.0Cu-0.5Mo	<ul style="list-style-type: none"> • Limited protective, stable growth followed by breakaway behavior in 0.5Cu • Similar behavior with Mo additions • High Cu content (1.0Cu) exhibits stable oxide growth with stable oxide transition 	<ul style="list-style-type: none"> • Breakaway corrosion in both 0.5Cu containing alloys • Possible stable behavior (nonbreakaway) in both 1.0Cu alloys but with high oxide growth rates
Zr-Nb	0.2Nb 0.4Nb 1.0Nb 1.5Nb 2.5Nb	<ul style="list-style-type: none"> • Higher protective oxide growth rates than observed in above alloys with transition element additions • 0.2Nb with lowest rate • No breakaway behavior 	<ul style="list-style-type: none"> • Protective behavior with no breakaway for all chemistries except 0.2Nb • High oxide growth rates
Zr-Nb-Sn	0.4Sn-0.2Nb 0.4Sn-0.4Nb	<ul style="list-style-type: none"> • Protective stable growth with oxide transition oxide growth 	<ul style="list-style-type: none"> • Nodular corrosion and non protective
Zr-Sn	0.4Sn 1.2Sn	<ul style="list-style-type: none"> • Protective stable growth with oxide transition oxide growth 	<ul style="list-style-type: none"> • Nodular corrosion and non protective
Reference	Pure Zr Zircaloy-4	<ul style="list-style-type: none"> • Nonprotective, spalling oxides in pure Zr following variable times of protective behavior • Zircaloy-4 exhibit stable oxide growth with multiple oxide transitions indicative of a layered oxide structure 	<ul style="list-style-type: none"> • Immediate breakaway behavior with white spalling oxide for pure Zr • Nodular to breakaway behavior in Zircaloy-4

the peaks associated with the tetragonal phase were smaller than those from the monoclinic phase by about a factor of 2.

The differences between the structure of protective and nonprotective oxides were most apparent at the oxide-metal interface, but some differences were also observed in the overall oxide texture. These differences were observed both between protective and nonprotective oxides formed on different alloys, or in the same alloy at different stages of the corrosion process, (after the oxide turns from protective to nonprotective).

Figure 6 shows a composite of intensity versus two-theta plots arranged as a function of distance from the oxide-metal interface. The peaks for the different phases are labeled. In the metal region, three hcp-Zr peaks are present with the $(0002)_{Zr}$ basal pole showing low intensity. After the oxide-metal interface, monoclinic ZrO_2 peaks are seen. The monoclinic oxide peak intensities deviate from those of a random monoclinic powder, indicating a strong texture in the oxide layer. For example, the ratio of the diffracted intensities of the $(\bar{1}11)_m$ and $(111)_m$ monoclinic oxide peaks is much lower than the 1.45 ratio observed in a random powder of monoclinic oxide. In particular, the oxide growth orientation is such that the poles of the $(200)_m$ oxide planes make a ~10 degree angle with the oxide growth direction and thus they are oriented close to perpendicular to the diffraction vector when the oxide is examined in cross section. As a result, the intensity of the $(200)_m$ peak is low, while the $(020)_m$ and $(002)_m$ peak intensities are high. In the bulk of the oxide, only one tetragonal peak is visible, the $(101)_t$ peak at 25.5 degrees two theta.

Figure 6 also illustrates the different structure seen at the oxide-metal interfaces in protective and nonprotective oxides. As previously observed in protective oxides layers formed in commercial alloys [4], diffraction peaks were observed both in the region of the metal ahead of the oxide-metal interface and in the adjacent oxide region. Figure 6(a) taken from an oxide layer formed on alloy Zr-0.2Fe-0.1Cr (H) during corrosion in water at 360°C illustrates the structure of a protective oxide. In particular, the peak shown at 28.7 degrees is present in the protective oxides, and absent in the nonprotective oxide layers. This

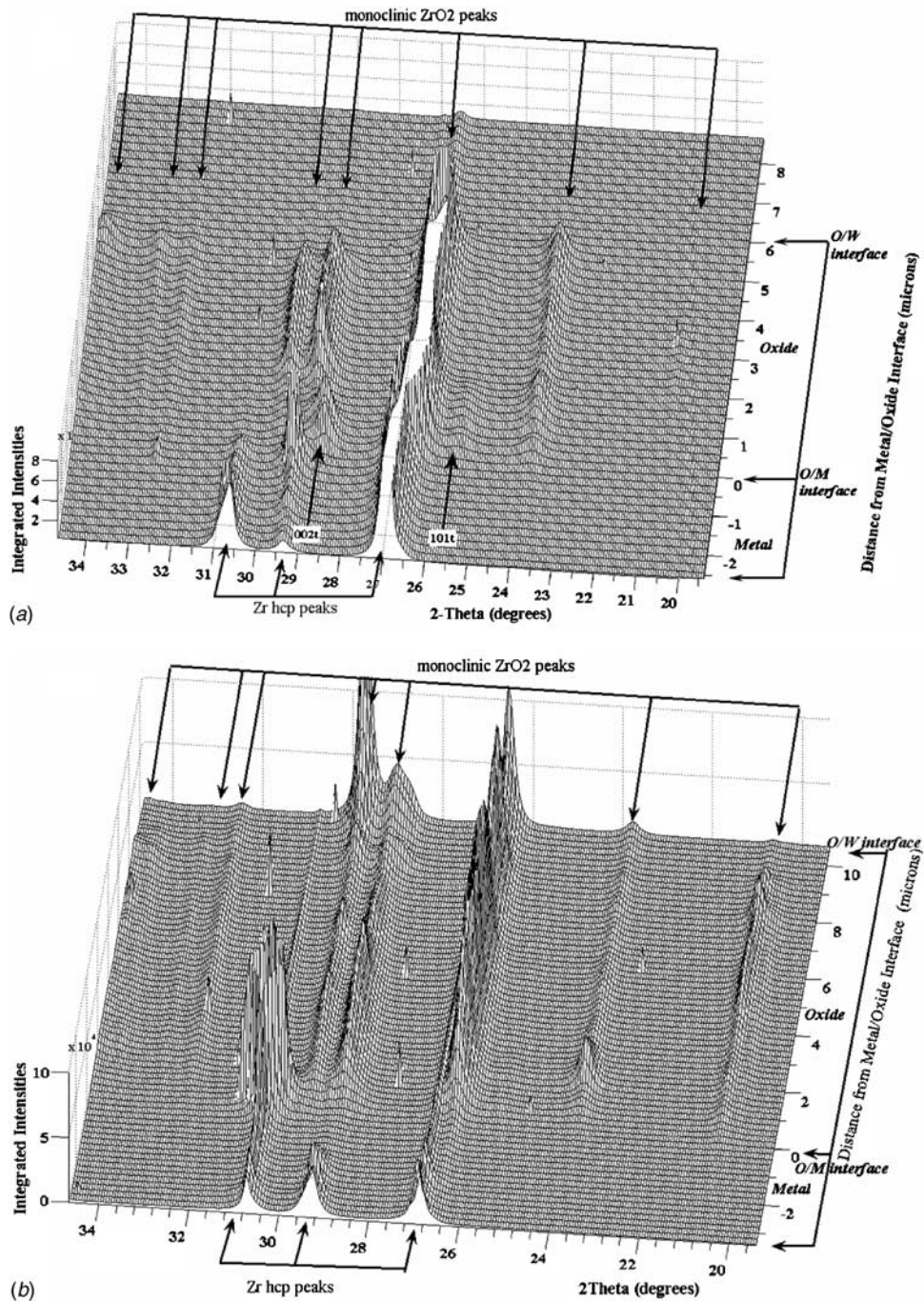


FIG. 6—X-ray diffracted intensity versus two-theta angle, plotted as a function of distance from the oxide-metal interface for (a) a protective oxide formed on Zr-0.2Fe-0.1Cr (H) after exposure to 360°C water for 415 days; (b) a nonprotective oxide formed on Zr-0.2Fe-0.1Cr (L) after exposure to 360°C water for 409 days.

peak has been identified previously as the (002)_t peak, belonging to a highly oriented tetragonal phase forming at the interface. As discussed below, the orientation relationships of this peak both with the metal and with the monoclinic phase into which it transforms suggest that this phase is a “precursor” phase, the presence of which allows the monoclinic phase to form in a more oriented fashion, and in a manner that minimizes stress accumulation in the oxide. This reduces the tendency for oxide breakup and loss of protective behavior. Figure 6(b) shows the structure of a nonprotective oxide layer formed on Zr-0.2Fe-0.1Cr (L) after 409 days in 360°C water. This oxide layer was initially protective and became nonprotective after 200 days. It can be seen that the oxide-metal interface does not exhibit the extra peak

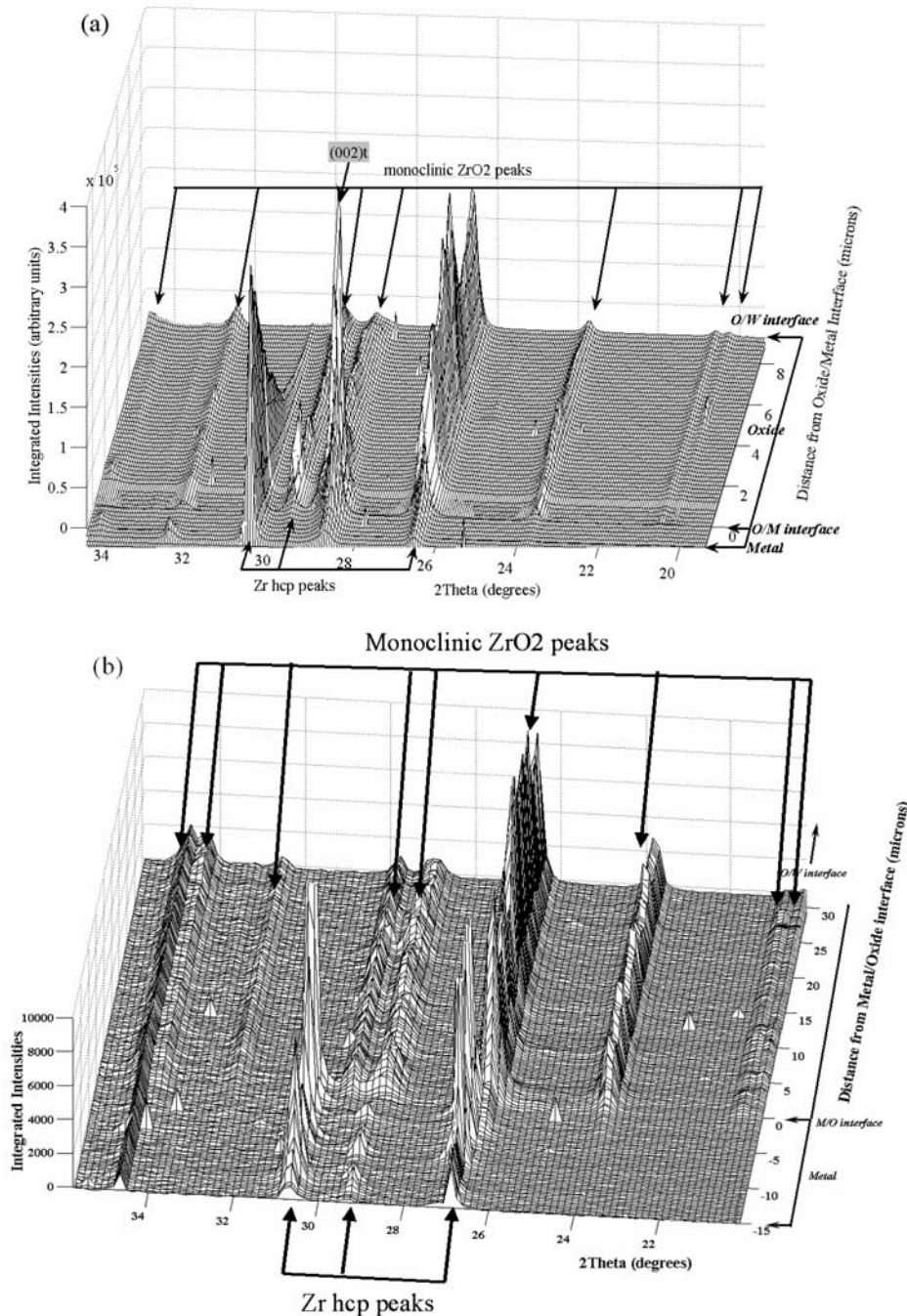


FIG. 7—X-ray diffracted intensity versus two-theta angle, plotted as a function of distance to the oxide metal interface for (a) an oxide formed on alloy Zr-0.2Fe-0.1Cr (H) after exposure to 500°C water for 150 days (weight gain 210.7 mg/dm²); (b) an oxide formed on alloy Zr-0.5Cr after exposure to 500°C steam for six hours (weight gain 724 mg/dm²).

intensities associated with the interfacial phases seen in the protective oxides, indicating that the monoclinic oxide forms directly from the metal without the intermediate tetragonal precursor phase.

This oxide-metal interface structure was also present in the oxide layers formed at 500°C, both in steam and in supercritical water. However, the intensity of the (002)_t peak was much more prominent in the oxide formed at 500°C than in the oxides formed at 360°C. Figure 7(a) shows a plot of diffracted intensity versus two-theta angle versus position in the oxide layer for a scan conducted on an oxide layer formed on Zr-0.2Fe-0.1Cr (H) after 150 days of exposure in supercritical water. This alloy maintains protective oxide growth in supercritical water up to 150 days. As can be seen, the (002)_t peak forms at the interface, with a much higher intensity than that of the same peak formed in 360°C water corrosion in the

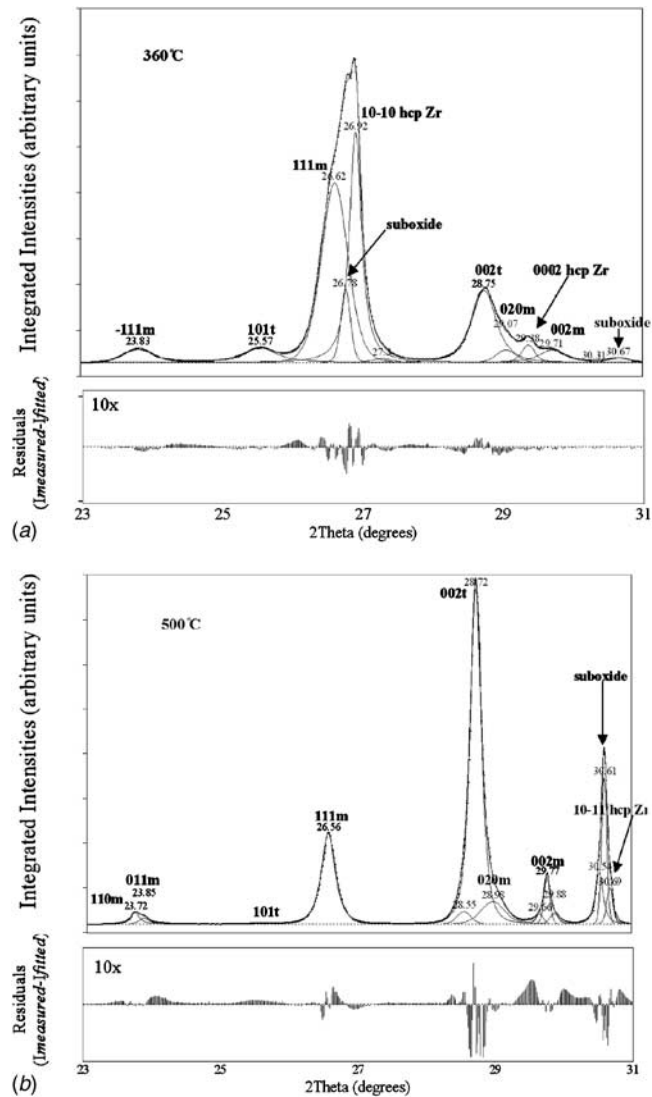


FIG. 8—X-ray diffracted intensity versus two-theta angle for a location near the oxide metal interface showing the peak fits performed, and the residuals for (a) Zr-0.2Fe-0.1Cr (H) exposed in water at 360°C (same sample as in Figure 6(a)) and (b) Zr-0.2Fe-0.1Cr (H), exposed in supercritical water at 500°C. Each peak location and corresponding (hkl) is also shown.

same alloy. Figure 7(b) shows a similar scan performed in a nonprotective oxide layer formed on alloy Zr-0.5Cr in 500°C steam. In this case, no interfacial phases are seen, and this was a universal observation for all nonprotective oxide layers studied.

The fact that the same oxide-metal interface structures are present in protective oxide layers formed during exposure to 360°C water and in 500°C steam or supercritical water indicates that similar mechanisms for forming protective oxides are present at both temperatures.

Quantitative Analysis of Diffraction Results

The diffraction results presented qualitatively in Figs. 6 and 7 were analyzed quantitatively by manually fitting the diffraction patterns with PeakFit software, using a Pearson VII peak shape. One example of the fitting process is shown in Fig. 8(a) which shows a fitted spectrum taken from the oxide-metal interface of a protective oxide layer formed in Zr-0.2Fe-0.1Cr (H) during exposure to 360°C water. The diffraction pattern shows the (002)_t peak seen only in the 0.3 micron region near the interface as well as the broad (101)_t peak associated with the normally observed tetragonal phase seen in the bulk of the oxide. It also shows the monoclinic oxide peaks. Figure 8(b) shows the same fitting performed for the oxide-metal interface of a Zr 0.2Fe-0.1Cr (H) alloy exposed to supercritical water at 500°C. A clear and strong (002)_t,

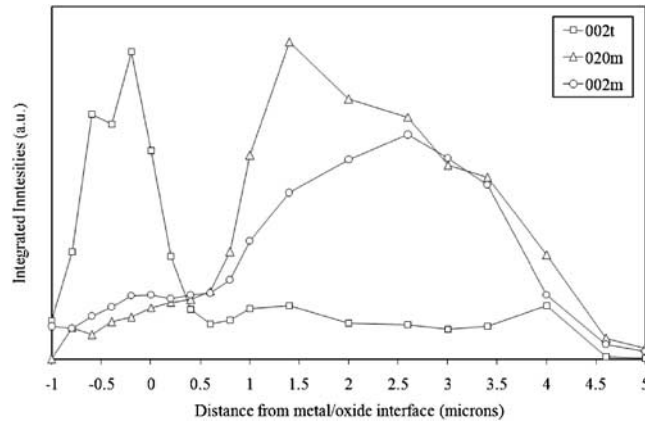


FIG. 9—Integrated peak intensities for the $(002)_t$, $(020)_m$ and $(002)_m$ peaks in the vicinity of the oxide-metal interface of sample Zr-0.2Fe-0.1Cr (H) shown in Fig. 6(a), as a function of distance from the oxide-metal interface.

peak is seen. Such an analysis yields the diffracted intensity for all the peaks as a function of location in the oxide as well as the full width at half-maximum from which the grain size can be calculated using the Scherrer equation [18]. As done previously [4], this determination needs to be performed away from the oxide metal interface to avoid strain broadening from the high stresses present at that location. The grain size measured in this case is perpendicular to the grain sides which are parallel to the sample surface. In the case of the columnar grains it is their width that is measured.

In addition to these differences, it is also possible to note in the protective oxide layers a significant intensity of the suboxide phase Zr_3O seen previously in the protective commercial alloys [5]. This is shown in Fig. 8, where the suboxide peaks are indicated. The suboxide peaks were seen at both temperatures but were more prominent at 500°C. A suboxide layer on the order of 3–5 microns is seen in the optical/SEM examination of the alloy oxides formed at 500°C [19], (much wider than the suboxide layers seen during examination of protective layers in commercial alloys corroded at 360°C, which were 0.1–0.5-micron thick). Other researchers have previously seen suboxide phases during zirconium alloy oxidation, e.g., Ref. [20].

Using the integrated intensities obtained from the fitted diffraction peaks, it is possible to plot the intensity of the various diffraction peaks against distance from the oxide-metal interface. Figure 9 shows the variation in the intensities of the $(002)_t$ peak from the highly oriented tetragonal phase, and the $(020)_m$ and $(002)_m$ peaks from the monoclinic oxide phase. From the figure it is clear that the intensity of the $(002)_t$ peak increases well before the intensities of the monoclinic peaks become significant, in agreement with the hypothesis that the $(002)_t$ peak belongs to a precursor phase for the monoclinic phase of the oxide. A similar distribution of peak intensities was observed in the oxides formed on Zircaloy-4, ZIRLO, and Zr-2.5 Nb, i.e., the $(002)_t$ peak of the tetragonal phase appeared a little before the oxide-metal interface and was only visible in a region of 0.2–0.5 microns near the interface.

Further evidence that the $(002)_t$ peak is different from the other diffraction peaks is shown in Fig. 10. Whereas Fig. 9 shows the integrated intensities of the peaks, the original diffraction pattern shows the appearance of the diffraction arcs before integration, as recorded in the CCD camera. On the left are the patterns obtained at the oxide-metal interface and on the right are the patterns taken 3 μm away, into the oxide. The top figure comes from a nonprotective (NP) oxide layer while the three lower figures are from protective oxides (P). The diffracted intensities associated with the $(002)_t$ peak are indicated with white arrows. These intensities are only observed at the interface of protective oxides.

It is clear that the peak associated with the $(002)_t$ intensity has a different appearance than the monoclinic peaks in the $\{200\}$ family. The diffraction intensity from this peak has a mottled appearance, in contrast with the even intensities seen along the arc for the monoclinic oxide peaks. It is also interesting to note in Fig. 10 that the intensities of $(002)_t$ and $(020)_m$ are strongly correlated, i.e., the peaks are aligned along the diffraction arc. This lends support to the idea that oxide grains which at the interface show a strong $(002)_t$ intensity grow to be monoclinic grains oriented according to the orientation relationship [7,21,22].

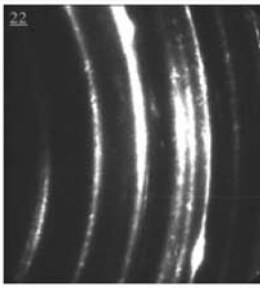
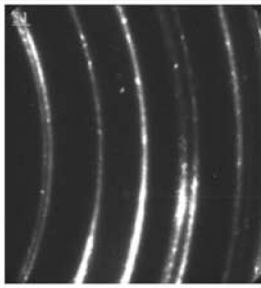
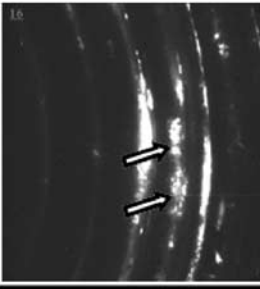
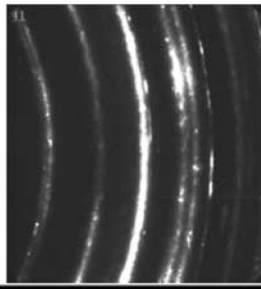
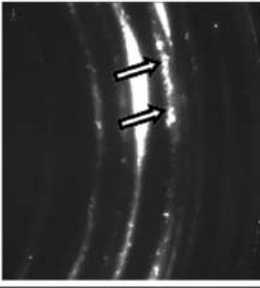
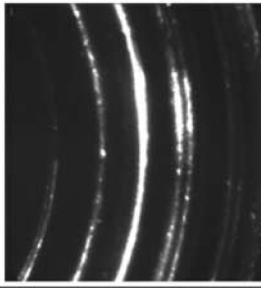
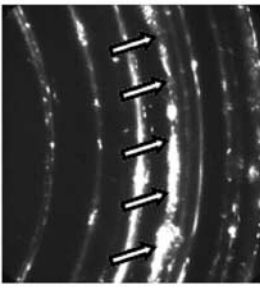
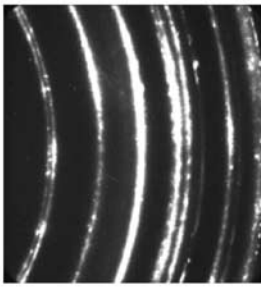
<i>Sample</i>	<i>Oxide/Metal Interface</i>	<i>3 μm into the oxide</i>
Zr-0.5Cr after 90 days in 360°C water Weight gain 955 mg/dm ² (NP)		
Zr-1.5Nb after 646 days in 360°C water Weight gain 130 mg/dm ² (P)		
Zr-0.2Fe-0.1Cr-H after 415 days in 360°C water Weight gain 55 mg/dm ² (P)		
Zr-1.0Cr-0.2Fe after 150 days in 500°C supercritical water Weight gain 422 mg/dm ² (P)		

FIG. 10—Diffraction patterns taken from oxide layers formed in four alloys, at the oxide metal interface (left) and 3 μm away (right) for (a) Zr-0.5Cr in 360°C water, (b) Zr-1.5Nb in 360°C water, (c) Zr-0.2Fe-0.1Cr (H) in 360°C water, (d) Zr-1.0Cr-0.2Fe in 500°C supercritical water (exposure times indicated). Arrows indicate the interfacial highly oriented tetragonal (002)_t peak found in the protective oxides.

$$(10\bar{1}1)_{Zr}/(002)_t/(020)_m \quad (2)$$

A more detailed texture analysis will be published elsewhere, but the overall texture of the protective and nonprotective oxides is different. This is demonstrated qualitatively by calculating the ratio of the average intensities of the $(\bar{1}11)_m$ and $(111)_m$ peaks. Figure 11 plots this calculated ratio for the various oxide layers, and labels the ratios as coming from a protective (P) or nonprotective (NP) oxide layer, according to the corrosion rate that was prevalent in the sample when it was archived. The protective oxides have a much smaller ratio than that of the nonprotective oxides. In fact, the ratio is the highest (closest to random) for the least protective oxide layers, with values of 0.9 and 0.8 for crystal bar and sponge Zr, respectively. As mentioned above, a random monoclinic powder has a ratio of 1.45, which means that the protective oxides are more heavily textured (farther from random) than the nonprotective oxides.

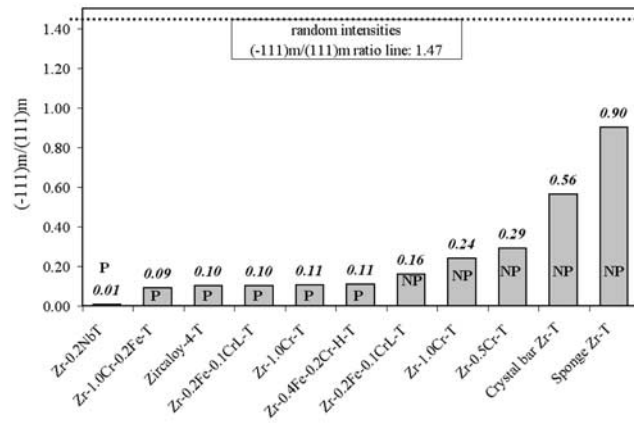


FIG. 11—Average ratio of the $(-111)_m$ and $(111)_m$ integrated oxide peaks from nonprotective (NP) and protective (P) oxide layers formed during corrosion in 360°C water, all taken from samples with the transverse orientation normal to the sample surface.

Finally, the tetragonal fraction in the oxide was calculated as a function of distance from the oxide-metal interface using the Garvie-Nicholson formula corrected for oxide texture [4,5,23,24]. Note that the Garvie-Nicholson formula uses the intensity of the $(101)_t$ peak to assess the tetragonal fraction, and thus it has no relation to the highly oriented tetragonal phase at the oxide metal interface mentioned above. The highest tetragonal fraction was 23 %, seen in the oxide layer formed in Zircaloy, and the lowest was 1.6 %, in the most corrosion resistant alloy, Zr-0.4Fe-0.2Cr (H). As discussed above, no relationship was found between the overall tetragonal fraction in the bulk of the oxide calculated by the Garvie-Nicholson formula and oxide protectiveness.

Discussion

The characteristics of protective and nonprotective oxides seen in this work are in agreement with previous observations made on commercial alloys. Figure 12 summarizes schematically the oxide structures seen in protective and non-protective oxides.

Figures 12(a) and 12(b) illustrate the distribution of diffraction peak intensities as a function of position relative to the oxide metal interface, in a protective and nonprotective oxide layer, respectively. The samples illustrated have the $(10\bar{1}0)$ Zr metal prism planes aligned with the surface of the sample (and thus have strong intensities), and the poles of the (0002) Zr metal planes within the plane of the surface of the sample (which implies low diffraction intensities). In the protective oxides (Fig. 12(a)) the interface exhibits strong Zr_3O suboxide peaks located at two-theta positions just below the α -Zr peaks. The ratio of the integrated intensities of the suboxide peaks to the corresponding α -Zr peaks was as high 1 to 1. In contrast, in the nonprotective oxides the suboxide peaks were either not present, or had lower intensities, on the order of 0.15–0.2 of the corresponding metal peaks.

The highly oriented tetragonal precursor phase indicated by the $(002)_t$ peak in Fig. 12(a) was not observed in the nonprotective oxides. When the $(002)_t$ peak was visible at the interface, the resulting texture in the bulk of the oxide resulted in a stronger intensity of the $(020)_m$ peak relative to that of the $(002)_m$ peak. In contrast for the nonprotective oxides the $(020)_m$ and $(002)_m$ peak intensities were nearly the same. The resulting texture also results in higher intensities of the $(111)_m$ peak relative to the $(-111)_m$ in the protective oxides as shown in Fig. 11.

Thus, the protectiveness of the oxide layer is associated with the presence of a highly oriented tetragonal oxide phase at the oxide-metal interface. This interfacial tetragonal oxide phase is believed to be a precursor phase which causes the monoclinic oxide to form in an orientation that minimizes stress accumulation during oxide growth [15]. The same association of the interfacial tetragonal phase with protective oxides was also seen in oxide formed at 500°C, both in supercritical water and in steam. The difference was the much higher volume fraction of the tetragonal interfacial phase for oxides formed at 500°C than in the oxides formed at 360°C.

Some negative observations can also be reported with some confidence. In particular, there is no

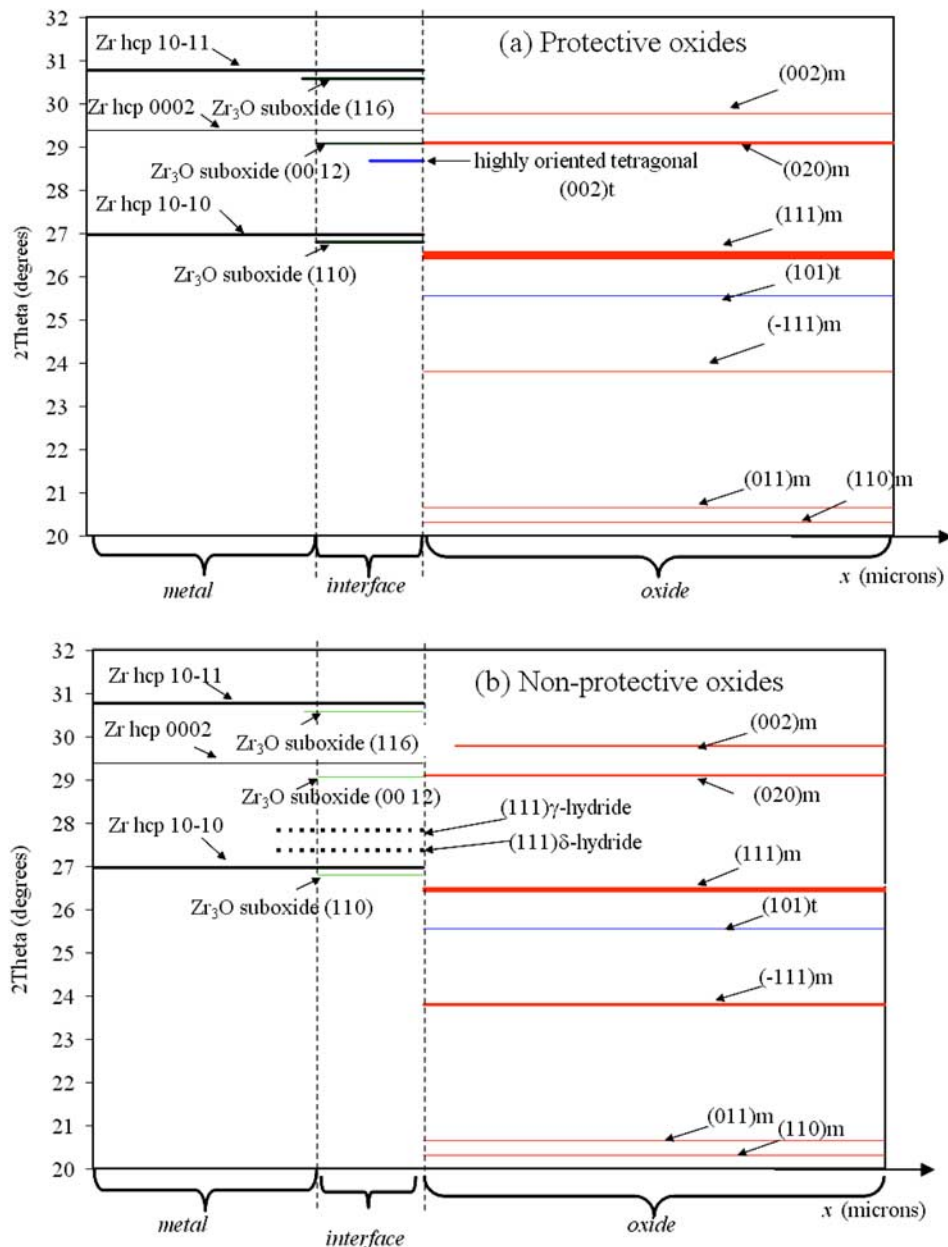


FIG. 12—Schematic plot of X-ray intensity versus two-theta angle as a function of distance from the oxide metal interface for (a) protective and (b) nonprotective oxide layers.

evidence that the overall tetragonal fraction, as measured by the Garvie-Nicholson equation, is associated with the formation of a protective oxide. For example, among the protective oxides formed at 360°C the highest tetragonal fraction was seen in Zircaloy-4, which, although protective, is not the most protective oxide. The most protective oxides (Zr-Fe-Cr alloys) exhibited maximum bulk tetragonal fractions (in the first micron near the oxide metal interface) of 5–7 % while that of Zircaloy-4 was ~20 %.

Thus, the highly oriented tetragonal phase, (present in the first 0.2 microns near the oxide-metal interface and visible through the (002)_t peak) is highly correlated with protective behavior while the bulk tetragonal phase (present to varying degrees throughout the oxide layer and visible through the (101)_t peak) is not correlated with protective behavior. It is emphasized that these are thought to be two different populations of tetragonal phase, the former transforming to monoclinic grains as soon as they reach a critical size [5] and the latter being a remnant phase, present in small amounts throughout the oxide.

There was also little evidence of periodicity in the oxides formed on alloys other than Zircaloy-4. However, this may be due to the fact that the oxide layers studied were not thick enough.

Since most previous X-ray diffraction studies of the oxide layers formed on zirconium alloys were

performed in frontal geometry (averaged over the whole oxide thickness) [16,17,25–27], it is only possible to compare the overall characteristics of the oxide layer texture and phase fraction and these correspond very well (oxide growth direction, overall texture and tetragonal fraction). The unique information shown in this work regarding the spatial distribution of phases in the oxide layer can only be compared to TEM studies, since these have high enough spatial resolution. Unfortunately, as pointed out previously, [28,29] the preparation of thin foils may destabilize phases such as the tetragonal phase which are stabilized by stress. Examination of the oxide layers by TEM in a similar study [6] shows features that are in agreement with the present observations.

Corrosion Kinetics

The detailed weight gain measurements obtained from the corrosion testing of the model alloys allow some conclusions to be drawn regarding the role of alloying elements in the process of the formation of a stable and protective oxide.

The first interesting result is that the pretransition corrosion kinetics are markedly different for the different alloys, ranging from near parabolic to lower than cubic. The question then arises as to what controls the corrosion kinetics. The overall corrosion reaction



can be broken down into several individual steps, each of which could be the rate limiting step. These steps include a surface reaction at the oxide-water interface, whereby oxygen is introduced into the layer, oxygen transport through the oxide (outward diffusion of Zr assumed not to occur), reaction at the oxide-metal interface and electron transport through the barrier layer.

Because the weight gain rate decreases as the oxide thickness increases, the rate limiting step necessarily involves transport of species through the oxide layer, so that the surface reactions cannot be rate limiting. Although it is normally assumed that the oxygen vacancy transport through the oxide layer (either by bulk diffusion or grain boundary diffusion) is rate limiting, it is possible that in some circumstances electronic transport is the rate limiting step, as discussed in the following.

The model of vacancy transport controlled corrosion in a homogeneous medium (either through the grain boundaries or through the bulk of the oxide) yields parabolic kinetics, i.e., $n=0.5$. The current results indicate that such a model may only be applicable to Zr-Nb alloys, which show $n \approx 0.45$. The corrosion kinetics in alloys containing transition metals show lower values of n ($n=0.2$ to 0.25) so that this model does not apply. The question can then be posed as to why.

Previous explanations of supra-parabolic ($n < 0.5$) behavior have included grain boundary migration through a population of grains whose size increases with oxide thickness [30], formation of lateral cracks that impede diffusion, a changing thickness of the barrier layer [31], and the effect of stress on diffusion. However, all of these explanations have problems. For example, TEM studies [6] do not show the required grain size variation across the oxide and simple calculations show that stress can only make minor changes in the vacancy migration energy (the elastic strain energy accumulated in a monoclinic oxide at yield ($\sigma_y^2/2E$) corresponds to only 0.002 eV/atom).

This difference in corrosion kinetics between Nb containing and transition elements containing alloys could be due to the Nb in solution being incorporated in solid solution into the oxide as an aliovalent solute, providing greater electrical conductivity in the oxide, allowing easier electron transport and causing the corrosion process to be limited by the diffusion of oxygen vacancies. In contrast, in the transition element alloys the corrosion process may be controlled by electron transport. The Zr-transition metal alloys, such as Zr-Fe-Cr, Zr-Cr-Fe, and Zr-Cu, contain a very small amount of alloying elements in the metal matrix, such that the oxide conductivity is controlled by impurities in the metal matrix which are incorporated in solid solution in the oxide. As a result in the oxides formed on precipitate-bearing alloys, the conductivity of the oxide may be smaller, thus causing a corresponding decrease in the vacancy flux in the oxide layer to match. This is borne out by the fact that, while protective, the corrosion kinetics of Zr, Zircaloy-4, and Zr-Fe-Cr are all similar. This would mean that Sn does not play a similar role as Nb in the changing the conductivity of the layer, since there is plenty of Sn in solution in Zircaloy-4 (likely the difference is that Sn has a similar valence as Zr). In any circumstance, the supra-parabolic and indeed, supra-cubic behavior of the weight gain for the precipitate bearing alloys is not consistent with a diffusion-controlled process in an unvarying, homogeneous solid.

Loss of Protectiveness: The Oxide Transition and Breakaway

The loss of protectiveness that occurs at the oxide transition differs from breakaway corrosion in that the oxide recovers its protective character in the former, but not in the latter. It is useful, however, to discuss the two processes as arising from similar degradation mechanisms. It is interesting to note that alloys that have extensive solid solutions such as ZrNb and Zircaloy did not undergo breakaway corrosion, while many precipitate-only alloys, such as ZrCrFe alloys and ZrCuMo alloys, sooner or later underwent accelerated corrosion. The higher alloying content ZrFeCr alloys withstood the full length of the test without undergoing breakaway corrosion, but possibly the test was not run for enough time. Thus when ZrNb and Zircaloy undergo loss of protectiveness at transition, manage to recover the protective behavior.

A significant difference is seen in stability to breakaway of the oxides formed in alloys Zr-0.4Fe-0.2Cr and Zr-0.2Fe-0.1Cr. While the former did not undergo breakaway during this test the latter either went into immediate breakaway (500°C) or went into breakaway after about 200 days (360°C). In fact, in general, as long as the alloy contained Fe and an overall alloying content of at least 0.6 % they resisted breakaway for the duration of the test. It is likely that the volume fraction of precipitates plays a role in creating a precipitate distribution that creates a composite oxide conductivity that is laterally homogeneous. In the lower volume fraction precipitate alloys, small side to side variations in conductivity in the micron scale (such as can occur between prior beta grains and the rest of the material) can be magnified. This leads to a faster oxide layer advance in one region than in another, causing the oxide layer to crack as a result. The extreme version of this is shown in Fig. 2(d). When precipitates are present, the electronic conductivity they afford is higher than that provided by impurities and it is also more homogeneous, leading to more stable oxide growth.

Two main classes of mechanisms have been proposed to explain the oxide transition/breakaway: those based on a development of stresses followed by mechanical failure of the oxide [28,32], and those based on an accumulation of porosity during oxide growth which, at some critical value reaches a percolation condition (continuous access of water through the oxide layer) [33]. In either case, the result is the creation of easier access paths for the corroding medium (water) to reach the oxide metal interface where new oxide is being formed.

When the hcp-Zr reacts with oxygen to form monoclinic ZrO₂, there is an accompanying volume expansion of 56 %, caused by the difference in unit cell volumes between the oxide and the metal. Essentially all of this expansion is accommodated in the normal direction, such that 1 μm of metal consumed yields 1.56 μm of oxide. This is done nearly perfectly during corrosion of protective alloys as the measured oxide thickness is within a few percent of 1.56 times the consumed metal. However, even a small deviation of a few percent from this ideal behavior (thereby causing some lateral expansion to occur along with the vertical expansion) causes large stresses to develop that can eventually crack the oxide.

One additional difficulty is that such stress is compressive and would create lateral cracks (as observed), rather than the vertical cracks required to breach the oxide. It is possible, however, that the formation of the lateral cracks leads to the interconnection of existing pores, creating a percolating condition for the water to transverse the oxide.

Given the above picture and in light of the oxide characterization performed in this work, it is possible to understand why one oxide layer is more susceptible to breakaway than another. We interpret the ever present association seen in this work of the precursor oxide phase with protective oxides and its orientation relationship with the monoclinic oxide as evidence that this phase allows a more properly oriented oxide to grow, in a way that minimizes stress accumulation and therefore delays the oxide transition to larger oxide thicknesses.

As for the reason why some oxides recover from transition and restart forming protective oxide while others go into breakaway, this may be related to the microchemical structure of the alloy and to how laterally homogeneous the alloy chemistry is. In the solid solution alloys (which do not undergo breakaway) the presence of the aliovalent solutes allows for the corrosion to be limited only by vacancy transport and for the transport through the oxide layer to be laterally homogeneous. Thus when the oxide loses protectiveness, a homogeneous protective layer is formed that re-establishes the pretransition kinetics. In the precipitate bearing alloys, it is possible that, at transition, statistical variations in precipitate distribution cause oxide advance to happen faster in one region than the other (at the micron scale). According to this hypothesis, a very homogeneous fine distribution of precipitates would be the most stable microstructure against breakaway.

Conclusions

A systematic study has been performed of oxide layers formed in model alloys during exposure to 360°C water and 500°C supercritical water and steam, using microbeam synchrotron radiation diffraction and fluorescence. The main conclusions are as follows.

- (a) Although the alloys studied were all tested in the same autoclaves, a wide variation in corrosion kinetics and oxide stability was observed among the model alloys studied, indicating that the alloy chemistry and microstructure determine corrosion behavior. The same alloys that showed protective behavior at 500°C also showed protective behavior at 360°C indicating that the mechanisms of corrosion and protective oxide formation are similar.
- (b) In the pretransition regime, the values of the weight gain coefficient n were observed to vary between $n=0.25$ and 0.45 at 360°C and between 0.33 and 0.6 at 500°C depending on the alloy. The solid solution alloys exhibited higher values of n than did the precipitates bearing alloys.
- (c) Microbeam X-ray diffraction examination of cross-sectional oxide samples identified systematic differences between protective and nonprotective oxides, especially at the oxide-metal interface. In the protective oxides an interfacial tetragonal oxide phase was observed, believed to be a precursor to the monoclinic oxide and which causes the oxide to form in a manner that maximizes occupation and minimizes stress accumulation, leading to more stable oxide growth.

Acknowledgments

The authors would like to acknowledge our partners, the University of Michigan and KAERI, who generated some of the corrosion data used in this study and with whom we had many productive discussions. We acknowledge the assistance of A. Siwy and J. Chaffee at Penn State in performing some of the diffraction pattern fits in this work. This research was supported by a DOE I-NERI grant no. DE-FG07-03RL14530. Use of the Advanced Photon Source was supported by the U.S. Department of Energy, Basic Energy Sciences, Office of Science, under Contract No. W-31-109-Eng-38. M. Gomes da Silva was a recipient of a scholarship from CNPq-Brazil for his doctoral study, while working on this project.

References

- [1] Yang, R., Ozer, O., and Rosenbaum, H., "Current Challenges and Expectations of High Performance Fuel for the Millenium," *Light Water Reactor Fuel Performance Meeting*, Park City, Utah, American Nuclear Society, 2000.
- [2] Sabol, G. P., Kilp, G. R., Balfour, M. G., and Roberts, E., "Development of a Cladding Alloy for High Burnup," *8th International Symposium on Zirconium in the Nuclear Industry*, ASTM STP 1023, ASTM International West Conshohocken, PA, 1989, pp. 227–244.
- [3] Mardon, J. P., Charquet, D., and Senevat, J., "Influence of Composition and Fabrication Process on Out-of-pile and In-pile Properties of M5 Alloy," *12th International Symposium on Zr in the Nuclear Industry*, ASTM STP 1354, ASTM International, West Conshohocken, PA, 2000, pp. 505–524.
- [4] Yilmazbayhan, A., Motta, A. T., Comstock, R. J., Sabol, G. P., Lai, B., and Cai, Z., "Structure of Zirconium Alloy Oxides Formed in Pure Water Studied with Synchrotron Radiation and Optical Microscopy: Relation to Corrosion Rate," *J. Nucl. Mater.*, Vol. 324, 2004, pp. 6–22.
- [5] Motta, A. T., Yilmazbayhan, A., Comstock, R. J., Partezana, J., Sabol, G. P., Cai, Z., and Lai, B., "Microstructure and Growth Mechanism of Oxide Layers Formed in Zr Alloys Studied with MicroBeam Synchrotron Radiation," *J. ASTM Int.*, Vol. 2, 2005, Paper ID JAI12375.
- [6] Yilmazbayhan, A., Breval, E., Motta, A., and Comstock, R., "Transmission Electron Microscopy Examination of Oxide Layers Formed in Zr Alloys," *J. Nucl. Mater.*, Vol. 349, 2006, pp. 265–281.
- [7] Yilmazbayhan, A., "Microstructural Basis of Uniform Corrosion in Zr Alloys," Ph.D. Thesis in Nuclear Engineering, Penn State University, 2004.
- [8] Barberis, P., Ahlberg, E., Simic, N., Charquet, D., Dahlback, M., Limback, M., Tagstrom, P., Lemaignan, C., Wikmark, G., and Lehtinen, B., "The Role of Second Phase Particles in Binary Zirconium Alloys," *13th International Symposium on Zirconium in the Nuclear Industry*, ASTM STP 1423, ASTM International, West Conshohocken, PA, 2002, p. 33.

- [9] Motta, A. T. and Jeong, Y. H., "Advanced Corrosion Resistant Zr Alloys for Use in High Burnup and Generation IV Systems," I-NERI Research Project, ROK-USA, 2003–2006.
- [10] Motta, A., Yilmazbayhan, A., Gomes da Silva, M. J., Comstock, R. J., Was, G., Busby, J., Gartner, E., Peng, Q., Jeong, Y. H., and Park, J. Y., "Zirconium Alloys for Supercritical Water Reactor Applications: Challenges and Possibilities," *J. Nucl. Mater.*, Vol. 371, 2007, pp. 61–75.
- [11] Erwin, K. T., Delaire, O., Motta, A. T., Birtcher, R. C., Chu, Y., and Mancini, D., "Observation of Second-phase Particles in Bulk Zirconium Alloys Using Synchrotron Radiation," *J. Nucl. Mater.*, Vol. 294, 2001, pp. 299–304.
- [12] Jeong, Y. H., Park, J. Y., Kim, H. G., Busby, J. T., Gartner, E. L., Atzmon, M., Was, G. S., Comstock, R., Gomes da Silva, M. J., and Motta, A. T., "Corrosion of Zirconium Based Fuel Cladding Alloys in Supercritical Water," *12th International Conference on Environmental Degradation of Materials in Nuclear Power Systems—Water Reactors*, NACE (National Association of Corrosion Engineering), 2005, pp. 1369–1377.
- [13] Hutchinson, B. and Lehtinen, B., "A Theory of the Resistance of Zircaloy to Uniform Corrosion," *J. Nucl. Mater.*, Vol. 217, 1994, pp. 243–249.
- [14] Bossis, P., Pecheur, D., Hanifi, K., Thomazet, J., and Blat, M., "Comparison of the High Burnup Corrosion on M5 and Low Sn Zircaloy-4," *J. ASTM Int.*, Vol. 3, 2006, Paper ID JAI12404.
- [15] Li, H., Glavicic, H. M., and Spuznar, J. A., "A Model of Texture Formation in ZrO₂ Films," *Mater. Sci. Eng., A*, Vol. A366, 2004, pp. 164–174.
- [16] Petigny, N., Barberis, P., Lemaignan, C., Valot, C., and Lallemand, M., "In situ XRD Analysis of the Oxide Layers Formed by Oxidation at 743 K on Zircaloy-4 and Zr-1NbO," *J. Nucl. Mater.*, Vol. 280, 2000, pp. 318–330.
- [17] David, G., Geschier, R., and Roy, C., "Etude de la croissance de l'oxyde sur le zirconium et le zircaloy-2," *J. Nucl. Mater.*, Vol. 38, 1971, pp. 329–339.
- [18] Cullity, B. D., *Elements of X-ray Diffraction*, Addison-Wesley, Reading, MA, 1978.
- [19] Peng, Q., Gartner, E., Busby, J. T., Motta, A. T., and Was, G. S., "Corrosion Behavior of Model Zirconium Alloys in Deaerated Supercritical Water at 500 C," *Corrosion*, Vol. 63(6), 2007, pp. 577–590.
- [20] Bossis, P., Lelievre, G., Barberis, P., Iltis, X., and Lefebvre, F., "Multi-Scale Characterization of the Metal-Oxide Interface of Zirconium Alloys," *12th International Symposium on Zirconium in the Nuclear Industry*, ASTM STP 1354, ASTM International, West Conshohocken, PA, 2000, p. 918.
- [21] Subbarao, E. C., Maiti, H. S., and Srivastava, K. K., "Martensitic Transformation in Zirconia," *Physica Status Solidii*, Vol. 21, 1974, pp. 9–39.
- [22] Yilmazbayhan, A., Motta, A. T., Kim, H. G., Jeong, Y. H., Park, J. Y., and Comstock, R., "Characterization of Oxides Formed on Model Zr Alloys in 360 C Water Using Synchrotron Radiation," *12th International Conference on Environmental Degradation of Materials in Nuclear Power Systems—Water Reactors*, Snowbird, UT, NACE (National Association of Corrosion Engineering), 2005, pp. 201–210.
- [23] Garvie, R. C. and Nicholson, P. S., *J. Am. Ceram. Soc.*, Vol. 55, 1972, p. 303.
- [24] Garvie, R. C., "Stabilization of the Tetragonal Structure in Zirconia Microcrystals," *J. Phys. Chem.*, Vol. 82, 1978, pp. 218–224.
- [25] Roy, C. and David, G., "X-ray Diffraction Analysis of Zirconia Films on Zirconium and Zircaloy-2," *J. Nucl. Mater.*, Vol. 37, 1970, pp. 71–81.
- [26] Valot, C., Ciosmak, D., Mesnier, M. T., and Lallemand, M., "Phase Analysis by Variable-Incidence X-ray Diffraction: Application to Zirconium Oxidation," *Oxid. Met.*, Vol. 48, 1997, pp. 329–345.
- [27] Penelle, R., Boisot, P., Beranger, G., and Lacombe, P., "Influence de l'orientation de monocristaux de zirconium sur les textures de croissance de la zircone monoclinique," *J. Nucl. Mater.*, Vol. 38, 1971, pp. 340–342.
- [28] Godlewski, J., Gros, J. P., Lambertin, M., Wadier, J. F., and Weidinger, H., "Raman Spectroscopy Study of the Tetragonal-to-Monoclinic Transition in Zirconium Oxide Scales and Determination of Overall Oxygen Diffusion by Nuclear Microanalysis of ¹⁸O," *9th International Symposium on Zr in the Nuclear Industry*, ASTM STP 1132, ASTM International, West Conshohocken, PA, 1991, pp. 416–436.
- [29] Godlewski, J., "How the Tetragonal Zirconia is Stabilized in the Oxide Scale That is Formed on a

Zirconium Alloy Corroded at 400 C in Steam,” *10th International Symposium on Zr in the Nuclear Industry*, ASTM STP 1245, ASTM International, West Conshohocken, 1994, pp. 663–686.

- [30] Sabol, G. P. and Dalgaard, S. B., “The Origin of the Cubic Rate Law in Zirconium Alloy Oxidation,” *J. Electrochem. Soc.*, Vol. 122, 1975, p. 316.
- [31] Barberis, P. and Frichet, A., “Characterization of Zircaloy-4 Oxide Layers by Impedance Spectroscopy,” *J. Nucl. Mater.*, Vol. 273, 1999, pp. 182–191.
- [32] Bradhurst, D. H. and Heuer, P. M., “The Influence of Oxide Stress on the Breakaway Oxidation of Zircaloy-2,” *J. Nucl. Mater.*, Vol. 37, 1970, p. 35.
- [33] Cox, B., “Some Thoughts on the Mechanisms of In-reactor Corrosion of Zirconium Alloys,” *J. Nucl. Mater.*, Vol. 336, 2005, pp. 331–368.